

Interacting Kerr-Newman Electromagnetic Fields

Sajad Aghapour¹, Lars Andersson², Kjell Rosquist³, and Tomasz Smolka⁴

¹Max Planck Institute for Gravitational Physics (Albert Einstein Institute), D-14476
Potsdam, Germany

²Beijing Institute of Mathematical Sciences and Applications, Beijing 101408, China

³Department of Physics, Stockholm University, Albanova University Center, SE-106 91
Stockholm, Sweden

⁴Department of Mathematical Methods in Physics, Faculty of Physics, University of
Warsaw, Pasteura 5, 02-093, Warsaw, Poland

May 22, 2024

Abstract

In this paper, we study some of the properties of the $G \rightarrow 0$ limit of the Kerr-Newman solution of Einstein-Maxwell equations. Noting Carter's observation of the near equality between the $g = 2$ gyromagnetic ratio in the Kerr-Newman solution and that of the electron, we discuss additional such coincidences relating to the Kerr-Newman multipoles and properties of the electron. In contrast to the Coulomb field, this spinning Maxwell field has a finite Lagrangian. Moreover, by evaluating the Lagrangian for the superposition of two such Kerr-Newman electromagnetic fields on a flat background, we are able to find their interaction potential. This yields a correction to the Coulomb interaction due to the spin of the field.

1 Introduction

This work is inspired by certain special properties of solutions of the Einstein-Maxwell field equations of general relativity. As noted by Carter [1], the Kerr-Newman solution has the same g -factor (gyromagnetic ratio) $g = 2$, as the electron (apart from the small correction to its value in quantum field theory)¹. When comparing the electron with the Kerr-Newman solution, the quantities involved are the gravitational parameters, the mass M and the spin parameter $a = J/M$ where J is the angular momentum, and the electromagnetic parameters, the charge Q and the magnetic moment μ . For the electron, the gravitational parameters are related by the inequality $a > M$ (actually $a \gg M$). This puts the comparison in the “over-extreme” part of the family of Kerr-Newman solutions. In this context, it is worth pointing out that over-extreme ($a > M$) objects are ubiquitous, ranging from elementary particles to the solar system, see Figure 1.

The limit $G \rightarrow 0$ of the Kerr-Newman solution yields a special solution of the Maxwell equations, known as the *magic field*. The term “magic” as coined by Lynden-Bell [3] refers to the separability of motion in the field. The separability is due to the existence of a Killing tensor (of 2nd order) in the Kerr-Newman geometry [4]. Lynden-Bell discussed some physical and mathematical properties of the magic field, in particular, whether it could be due to a charge distribution. We will instead consider the magic field as a primary entity by itself and investigate the interaction between two magic fields.

The above-mentioned coincidence of the g -factors of the electron and the Kerr-Newman solution is actually a special case of related coincidences of the gravitational and electromagnetic multipoles of the Kerr-Newman solution and the known multipoles of the electron. The non-zero electromagnetic multipoles of the magic field coincide with those of the Kerr-Newman field. The experimentally measured values of the electron are in close agreement with five of the first ones in the two series of multipoles, electromagnetic and gravitational. They are the three first electromagnetic multipoles (charge: $q_0 = Q$, electric dipole: $q_1 = 0$, magnetic moment: $\mu_1 = Qa$) and the first and third gravitational multipoles (mass: $m_0 = M$ and angular momentum:

¹The quantum field theory correction of the g -factor is $\Delta g = \alpha/2\pi \approx 0.001$ where α is the fine structure constant [2].

Typical spin values

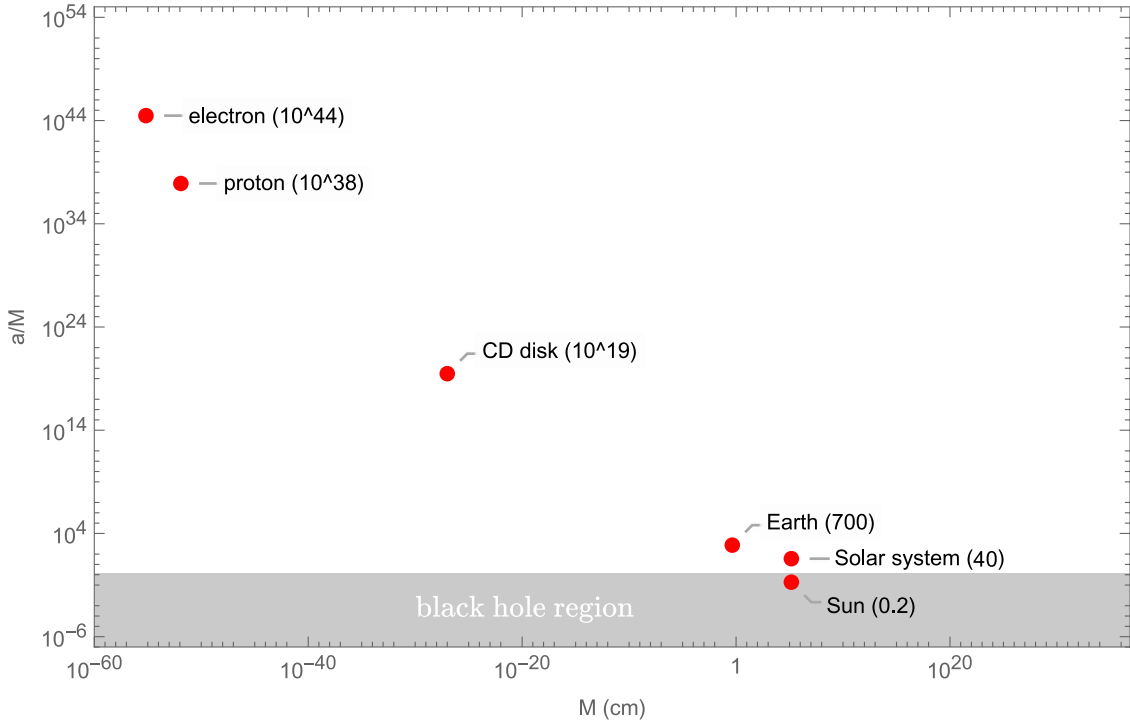


Figure 1: Values of the spin parameter a/M vs. mass (by order of magnitude) for objects with sizes ranging from the electron to the solar system. The value for a CD disk is calculated from the value 10^{18} for a 33 rpm vinyl LP record given by Dietz and Hoenselaers [5]. The astronomical values are calculated from [6].

$j_1 = Ma$). In particular, precise measurements of a possible electric dipole moment of the electron have so far been consistent with a zero value [7, 8].

The multipole structure of the Kerr-Newman electromagnetic field consists of alternating electric and magnetic multipoles, i.e. electric monopole (i.e. charge), magnetic dipole, electric quadrupole etc., compare Table 1. The multipole structure of its gravitational field has a similar structure of alternating gravitoelectric and gravitomagnetic multipoles, i.e. gravitoelectric monopole (i.e. mass), gravitomagnetic dipole (i.e. angular momentum), gravitoelectric quadrupole etc., compare Table 2.

It is also notable that the g -factor agreement depends on a certain combination of the Kerr-Newman multipoles. To see this, note that the g -factor is defined by the relation

$$g = 2 \frac{\Theta}{a} \quad (1.1)$$

where $\Theta = \mu/Q$ is the magnetic dipole moment per unit charge and $a = J/m$ is the angular momentum per unit mass. Expressed in terms of multipole moments, the g -factor has the form

$$g = 2 \frac{m_0 \mu_1}{q_0 j_1} \quad (1.2)$$

where the subindices refer to the multipole order; cf. Tables 1 and 2.

The next interesting electromagnetic multipole is the electric quadrupole, which has not been measured for the electron. By the Wigner-Eckart theorem [9], a spin-1/2 particle like the electron in flat space is expected to have a vanishing electric quadrupole moment. In contrast, the quadrupole moment of the magic field is non-vanishing. As we shall see, cf. section 2.1 below, the magic field lives in a locally flat but topologically non-trivial spacetime, which has a ring-like, conical singularity with a 2π angle excess, giving the magic field a spin-1/2 aspect. In this context, it is worth pointing out that Compton found a ring-like structure for the electron [10]. This may be taken as an indication of an oblate spheroidal structure of the electromagnetic field of the electron. Compare also the more recent paper [11]. The magic field originates in the Kerr-Newman solution, i.e., in a classical gravitational context, where the Wigner-Eckart theorem does not apply. Similarly,

viewing the electron as a gravitating object is outside the range of validity of the Wigner-Eckart theorem, cf. [12].

l	Name	Electric (q_l)	Magnetic (μ_l)
0	monopole	Q^*	
1	dipole	q_1	μ^*
2	quadrupole	q_2	μ_2
3	octupole	q_3	μ_3
...

Table 1: The electromagnetic multipoles $\mathcal{E}_l = q_l + i\mu_l$. The non-vanishing electromagnetic multipoles of the Kerr-Newmann solution are in the cells with thick borders (yellow cells in the color version of the paper). The starred moments, i.e. the electric charge Q and magnetic dipole μ , are the only measured electromagnetic multipoles of the electron. The gray cell stands for a (unphysical) magnetic monopole, that we do not consider in this work.

l	Name	Gravito-electric (m_l)	Gravito-magnetic (j_l)
0	monopole	M^*	
1	dipole	m_1	$J (= Ma)^*$
2	quadrupole	m_2	j_2
3	octupole	m_3	j_3
...

Table 2: The gravitational multipoles $\mathcal{G}_l = m_l + ij_l$. The non-vanishing gravitational multipoles of the Kerr-Newmann solution are in cells with thick borders (yellow in the color version of the paper). The starred moments, i.e. the mass M and (spin) angular momentum J , are the only measured gravitational multipoles of the electron. The gray cell stands for the NUT solution, which is not relevant in the context of this work.

As is well known, even for the single magic field, its complete analytic continuation is not globally Minkowski. The corresponding topology has, in fact, two asymptotic ends, which are connected by two gates². The gates have the form of two circular disks, both of which are bounded by the (single!) ring singularity appearing in the oblate spheroidal coordinates of R^3 . To illustrate this structure, consider a curve in one of the sheets starting from a point P at one of the disks and passing around the singularity by an angle 2π to reach the other disk. To actually close the curve, one needs to pass that through that gate and pass another 2π angle on the other sheet. The curve can then be closed, having traversed an angle 4π around the singular ring. Such a curve cannot be shrunk to a point without cutting, which means that the line/curve has different topological properties than those of the curves that lie only in one of the sheets. This topological structure gives one more analogy to the electron by reference to its spin-one-half nature.

A notable fact about the magic field is that it can be obtained by making an imaginary translation of a Coulomb field in a spacelike direction. Such a procedure was described already by Appell in 1887 [13], cf. also [14–16]. This procedure is closely related to the well-known Newman-Janis algorithm [17]. This involves a coordinate complexification process that transforms a static spacetime into a rotating one. Originally, the algorithm has been used to obtain the Kerr metric from the Schwarzschild and later the Kerr-Newman solution from Reissner-Nordström.

The complex deformation process (complex shift) has been examined recently from the perspective of scattering amplitudes in [18]. This study analyzes the impulse imparted to a test particle by a heavy spinning particle, both in electromagnetic and gravitational contexts. In the electromagnetic case, the impulse due to the magic field (termed “ $\sqrt{\text{Kerr}}$ ”) is shown to be reproduced by a charged spinning particle, with the

²Although the existence of two asymptotic ends has been discussed by a number of authors, both for the Kerr-Newman geometry and the magic field, it seems that the fact that there are two gates has not been appreciated in earlier works.

shift in the Coulomb potential corresponding to the exponentiated spin-factor in the amplitude. Based on a comparison of the result with the corresponding calculation using the scattering amplitudes, they argue that the complex shift corresponds to the exponentiation of spin operators in the large-spin limit.

Another relation between the electromagnetic magic field and the Kerr metric is through the (classical) double copy formalism, which is the origin of the nomenclature “ $\sqrt{\text{Kerr}}$ ” for the magic field. In this approach, a specific class of solutions of General Relativity that admit a Kerr-Schild form introduce solutions of Maxwell theory (or non-Abelian Yang-Mills theory in a more general setting). Through this correspondence, the Schwarzschild metric is the double copy of the Coulomb solution, and the Kerr metric is the double copy of the magic field [19]. This relation is used in [18] for the gravitational case to derive the impulse due to a Kerr black hole for gravitationally coupled spinning particles.

Our main object in this work has been to study interactions of magic fields at the classical level using only the magic fields themselves. This involves representing interactions in terms of localized fields rather than particles or currents. This is in contrast to the standard textbook way of dealing with classical interactions, namely, taking the particles for granted and subjecting them to fields that can be external or generated by other particles. In the textbook Lagrangian or Hamiltonian picture, the particle aspects are represented by the kinetic energy while the potentials represent the fields. Our starting point is to write down a pure field Lagrangian, which will nevertheless represent both field and particle aspects. The Lagrangian is defined as a superposition of the localized fields. These fields will, by assumption, be constructed from the magic field solutions mentioned above. Such solutions will then be valid in a flat spacetime, which is locally Minkowski but not necessarily globally Minkowski.

While our treatment is purely classical, as mentioned above, one can nevertheless make certain valid comparisons with properties of the electron and a single magic field. Turning now to the treatment of interactions of two magic fields, we have obtained effective interaction potentials for some cases. The potentials we have calculated are for aligned spins on a common axis (up-down case) and for parallel spins based on a common plane perpendicular to the spins (side-by-side case). The structure of the potentials leads to possibilities to study “magic” type electron-electron and electron-positron interactions. In particular, in the up-down magic electron-positron case with opposite charges, there appears a state in which the fields are in equilibrium, see Figure 11b. The state is in equilibrium with respect to the direction of the aligned spins. To know if the state is a stable equilibrium, one can compare it with the side-by-side potential in Figure 11d. In that case, the potential walls indicate an attractive force when the separation of the fields is larger than the field separation in the up-down case, possibly indicating stability. Although we cannot rule out some intermediate channel between the two cases that would break stability at this stage, we consider this possibility to be unlikely.

To compare these results with actual physical electrons and positrons, we let the magic charges equal the elementary charge. Then, in the up-down equilibrium state, the distance between equilibrium positions turns out to be equal to twice the reduced Compton wavelength, see Figure 11.

In the following, we review the construction and essential properties of the magic electromagnetic fields in section 2. In particular, we discuss the topology of the analytic extension of its potential and continuity of the field in 2.1 and calculate the self-Lagrangian for a single magic field in 2.2. We analyze the interaction of two magic fields in section 3 in two specific configurations and discuss the results. Further discussions and concluding remarks are given in section 4.

2 Electromagnetic Magic Field

As we mentioned in the introduction, the electromagnetic magic field can be obtained in different ways. Each of these approaches demonstrates some of the extraordinary features of this field and its relation to other solutions of physically important field equations, such as Laplace, Maxwell, and Einstein. In this section, we adopt the simplest approach to obtain the magic field from the Coulomb solution by applying a complex transformation in one of the spatial directions. We then analyze the new solution and discuss the analytic continuation of the background space on which such a solution resides. In other words, we analyze the Riemann surface and find that the magic field as a complex function is continuous and single-valued. The result is the same as the one obtained from the other approach in which one takes the limit $G \rightarrow 0$ of the Kerr-Newman solution of the Einstein-Maxwell system. In the following sections, we will review the nontrivial topology of the magic field and pave the way for the analysis of the self-energy and interaction Lagrangians.

For our analysis in this paper, it is convenient to represent the electromagnetic field by the (complex)

Weber-Silberstein vector³,

$$\mathcal{F} = \mathbf{E} + i\mathbf{B} \quad (2.1)$$

satisfying the (free) Maxwell equations

$$\nabla \cdot \mathcal{F} = 0, \quad (2.2a)$$

$$i\partial_t \mathcal{F} - \nabla \times \mathcal{F} = 0. \quad (2.2b)$$

Restricting to stationary⁴ solutions, both \mathbf{E} and \mathbf{B} fields are curl-free (and hence also the Weber-Silberstein vector \mathcal{F}) and can be obtained from scalar potentials. We introduce the complex scalar potential \mathcal{Z} according to

$$\mathcal{F} = -\nabla \mathcal{Z}. \quad (2.3)$$

which generates the stationary solutions of Maxwell's equations (2.2). As a result of the (complex) Gauss equation (2.2a), the complex potential \mathcal{Z} satisfies the Laplace equation

$$\nabla^2 \mathcal{Z} = 0. \quad (2.4)$$

The simplest potential associated with a point charge q at the origin generating the Coulomb solution of Maxwell's equations is

$$\mathcal{Z} = \frac{q}{R}, \quad (2.5)$$

where $R = \sqrt{x^2 + y^2 + z^2}$ is the distance of a given point from the origin. This potential is also proportional to the fundamental solution of the Laplacian and therefore satisfies (2.4) everywhere outside the origin, where it is singular.

Following Appell [13] and Sommerfeld [14], we apply a complex translation $z \rightarrow z - ia$ to the Coulomb potential (2.5) to obtain the complex potential

$$\mathcal{Z} = \frac{q}{\sqrt{\chi^2 + (z - ia)^2}}, \quad (2.6)$$

where $\chi = \sqrt{x^2 + y^2}$ is the polar radius. Notice that we always mean the principal branch by the square root of a complex expression for which the real part is positive. The potential \mathcal{Z} in (2.6) is a complex combination of the electrostatic potential Φ and the magnetostatic potential Ψ as

$$\mathcal{Z} = \Phi + i\Psi. \quad (2.7)$$

This complex potential is, in fact, the electromagnetic (one of the pair of complex) Ernst potentials of the Kerr-Newman solution [22, 23]. The potential \mathcal{Z} in (2.6) generates the electromagnetic field of the form

$$\mathcal{F} = -\frac{q(\chi \partial_\chi + (z - ia) \partial_z)}{(\chi^2 + (z - ia)^2)^{3/2}}, \quad (2.8)$$

which has both non-vanishing electric and magnetic parts, contrary to the elementary Coulomb field.

Following Lynden-Bell, [24], we will refer to \mathcal{F} and \mathcal{Z} as the magic field and the magic potential, respectively. Similarly to its potential, the electromagnetic field is singular on the ring \mathcal{R} at $\chi = a$ on the $z = 0$ plane. This set is excluded from the domain. The field lines of electric and magnetic parts of the magic field, when viewed in Euclidean space, are displayed in Figure 2 below. The apparent discontinuity of the field on the disk spanned by the singular ring is removed by considering the analytic continuation of the field, cf. section 2.1. Under the reflection with respect to the $z = 0$ plane, the electric field is symmetric, while the magnetic field is anti-symmetric.

As mentioned in the introduction, the electromagnetic magic field can be obtained by taking the limit $G \rightarrow 0$ of the Kerr-Newman solution of the Einstein-Maxwell system. As a result of that limit, the background becomes locally flat with a non-trivial topology with two sheets, each having its own asymptotic region.

³Also known as the Riemann-Silberstein vector [20], cf. the footnote 114 in [21].

⁴An electromagnetic field \mathbf{F} is called stationary if it is preserved under the action of a time-like Killing vector field \mathcal{T} of the background $(\mathcal{M}, \mathbf{g})$, i.e. $\mathcal{L}_{\mathcal{T}}\mathbf{F} = 0$.

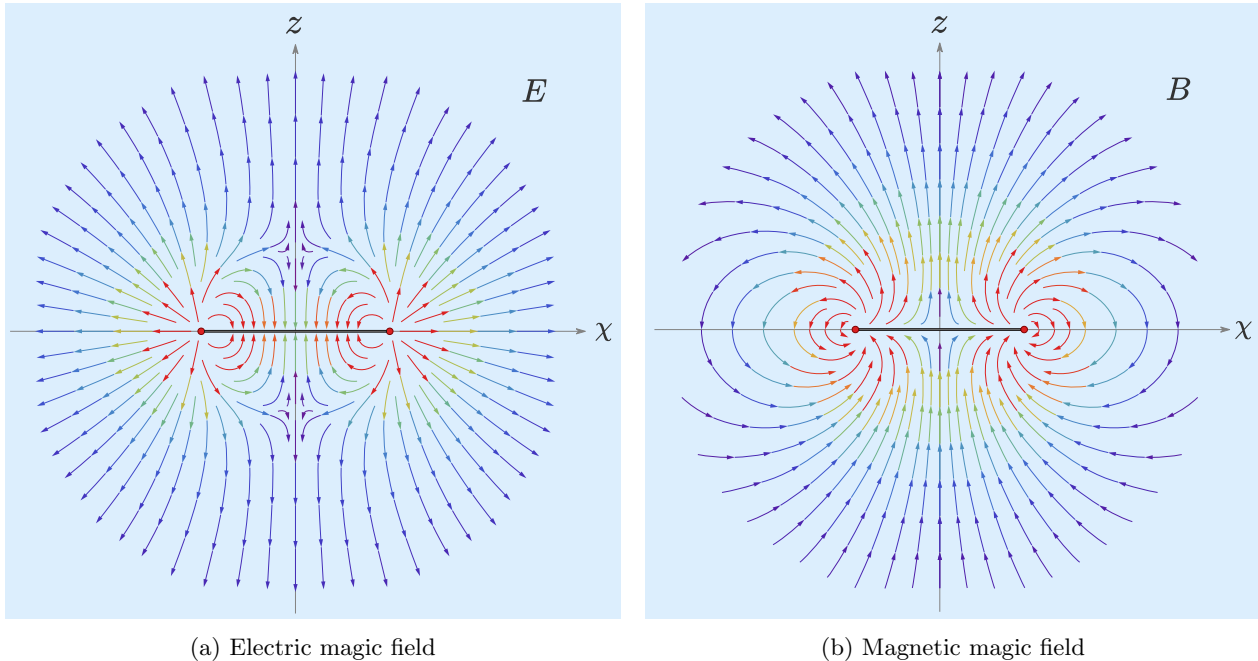


Figure 2: Electric and magnetic components of the magic field viewed in Euclidean space. The rainbow color-coding demonstrates the fields strengths, with red representing the extreme values and purple the negligible ones. The red points on the χ -axis display the singular ring \mathcal{R} intersections, and the line segment between them displays the intersection of the branch-cut disk \mathcal{D} spanned by the ring. The fields have azimuthal symmetry around the z -axis. The apparent discontinuity of the field on the disk spanned by the singular ring is removed by considering the analytic continuation of the field, cf. section 2.1.

However, the electromagnetic field of the solution remains intact in that limit, and it matches (2.8). In the subsequent section 2.1, we show how the analytic continuation of the potential (2.6) extends the primary domain, i.e. the Euclidean space without the ring \mathcal{R} , into a two-sheeted Riemann surface. The potential is only continuous and single-valued in this extension. We also verify that the topological structure of this Riemann surface indeed coincides with that of the Cauchy surfaces of the $G \rightarrow 0$ limit of the Kerr-Newman space-time.

Another approach to explain the discontinuity of the fields at disk \mathcal{D} taken by different researchers had been to try to find a source on the disk and the ring (see e.g. [3,25,26]). This approach leads to exotic sources with infinite charge and current densities rotating with the speed of light. We do not follow this approach and will instead use analytic continuation, thereby avoiding the problems with unphysical sources.

2.1 Analytic Continuation of the Magic Field

We begin our analysis by briefly discussing the complex square-root function, a lower-dimensional analog of the magic field. Recall that the complex square root function $f(\alpha) = \alpha^{1/2}$, where α denotes a complex variable, is double-valued over the complex plane. However, we can introduce a branch cut to make it single-valued. This process defines two separate branches of the function, which are discontinuous along the branch cut. The analytic continuation of the function across the branch cut connects two branches smoothly, resulting in a Riemann surface with two sheets glued appropriately along the branch cut. This Riemann surface, as the connected double cover of the complex plane, is the natural domain on which the square-root function is single-valued and continuous. There is no restriction on choosing the branch cut apart from the property that it connects the branch point at zero, where the value of the function agrees for both branches, to infinity. By convention, the principal branch cut is defined along the negative real axis, with the principal branch taking positive values on the positive real axis. This is our choice of branch cut in all analyses throughout this paper. For the inverse square root $\alpha^{-1/2}$ all above is valid, except that it is singular at the branch point at zero, and the Riemann surface is the connected double cover of the punctured complex plane.

For the square root in the magic field potential (2.6), which is a multivariable function, the set of branch

points is the singular ring \mathcal{R} at $\chi = a$ in the $z = 0$ plane, and the principal branch cut is the disk⁵ $\mathcal{D} = \{\chi < a, z = 0\}$ spanned by the ring singularity, where the real part of the radicand, i.e. the argument of the square root, is negative, and its imaginary part vanishes. Therefore, the Riemann surface \mathcal{V} of the magic potential consists of two sheets \mathcal{V}_1 and \mathcal{V}_2 glued together along the branch-cut disk \mathcal{D} . It possesses two distinct asymptotic regions, each associated with either of the sheets, and is punctured on the ring singularity.

The values of the potential function on two sheets of its Riemann surface \mathcal{V} are only different in overall sign. In other words, we can cover the second sheet with another copy of Cartesian coordinates so that the mapping between the two coordinate systems transforms the potential to its negative. Therefore, the potential on the whole Riemann surface in these two Cartesian coordinate systems can be written as

$$\mathcal{Z} = \frac{\pm q}{\sqrt{\chi_n^2 + (z_n - ia)^2}}, \quad n = 1, 2, \quad (2.9)$$

where each of the signs \pm is associated with either of the sheets \mathcal{V}_n . In order to make the potential \mathcal{Z} continuous along the branch-cut disk \mathcal{D} where $\chi_n < 0$ and $z_n = 0$, we need to glue the upper lip of the cut from the first sheet to the lower lip of the cut from the second sheet and vice versa. The two pairs of glued lips are two distinct gates between the sheets.

The gluing of the two sheets of the Riemann surface \mathcal{V} , in the way that we explained, requires the Cartesian coordinate systems that we used in (2.9) to have opposite orientations because the flipping is along one of the coordinates (i.e., z coordinate). We need a third coordinate system that covers the neighborhood around the branch cut in both sheets and overlaps with the two Cartesian coordinate systems to explore this and other nontrivial topological features. In the following, we will use the oblate spheroidal coordinates, extended by analytic continuation for this purpose.

The Riemann surface \mathcal{V} of the magic potential that was described earlier shares the topology of spatial hypersurfaces of the spacetimes discussed by Zipoy [27] and matches that of the $m \rightarrow 0$ limit of the maximal analytic continuation of the Kerr solution and $G \rightarrow 0$ limit of the Kerr-Newman solution [1, 23, 28]. This will be most evident when we introduce the oblate spheroidal coordinates to our analysis. The oblate spheroidal coordinates (r, θ, ϕ) are defined via the transformation

$$x = \sqrt{r^2 + a^2} \sin \theta \cos \phi, \quad y = \sqrt{r^2 + a^2} \sin \theta \sin \phi, \quad z = r \cos \theta, \quad (2.10)$$

in which we have $\chi = \sqrt{r^2 + a^2}$. Note that the oblate coordinates r and θ are different from the standard spherical radial and angular coordinates. Their level sets are, respectively, the spheroids and hyperboloids of revolution around the z -axis. Here r is the length of the semi-major axis of spheroids with their foci at the ring $\chi = a$ on the $z = 0$ plane and θ is the angle of asymptotes of the hyperboloid. On the principal branch, where we first obtained the magic potential (2.6), the oblate r -coordinate is a non-negative real number and $0 \leq \theta \leq \pi, 0 \leq \phi \leq 2\pi$. We will see that the extension of the r -coordinate to negative values enables the oblate coordinate system to cover the whole Riemann surface in a beneficial way.

The oblate spheroidal coordinates adapt very well to the singularity and topological structure of the Riemann surface of the magic field. The ring singularity \mathcal{R} of the magic potential (2.6), which is the branch point set of the square root, coincides with the focal ring of r -constant spheroids and the coordinate singularity at $\{r = 0, \theta = \pi/2\}$. The principal branch cut at the disk \mathcal{D} spanned by the ring \mathcal{R} is mapped into two separate disks at $\mathcal{D}_1 = \{r = 0, 0 \leq \theta < \pi/2\}$ and $\mathcal{D}_2 = \{r = 0, \pi/2 < \theta \leq \pi\}$. These are the two separate lips of the branch cut \mathcal{D} with the same boundary at the ring \mathcal{R} , which are to be glued “correctly” to their counterparts from the second sheet after the extension that we perform. We then denote the glued lips with \mathcal{D}_1 and \mathcal{D}_2 again, for obvious reasons, and call them the “gates” between the two sheets of the Riemann surface \mathcal{V} .

The analytic continuation that leads to the whole Riemann surface of the potential is the most straightforward in oblate spheroidal coordinates and needs only the continuation of the oblate r coordinate to include negative values to cover the second sheet. Therefore, the equations (2.10) give at once the transformation from both copies of the Cartesian (polar) coordinates used in (2.9). The big advantage of this is that the gluing of the sheets together is done correctly, as we need for the continuity of the potential over the branch cut lips (gates).

The validity of the coordinate transformation (2.10) on the whole Riemann surface \mathcal{V} , enables us to write the analytically continued magic potential \mathcal{Z} in (2.9) in oblate spheroidal coordinates as

$$\mathcal{Z} = \frac{\pm q}{\sqrt{(r - ia \cos \theta)^2}} = \frac{q}{r - ia \cos \theta}, \quad (2.11)$$

⁵Another choice of branch cut is a surface which connects the singular ring with the infinity. However, in this case, the potential (2.6) does not have vanishing asymptotics at infinity. In this context, the choice of branch cut on the disc \mathcal{D} is natural.

where in the last equality, the different signs from the square root simplification in either of sheets with $r \geq 0$ or $r \leq 0$ cancels the sign associated with the relevant sheet, and the last expression holds for the entire Riemann surface. The merit of exploiting the oblate spheroidal coordinates in covering the whole Riemann surface of the magic potential becomes evident again in the fact that the last simple result in (2.11) is obviously continuous on the two gates $\mathcal{D}_1 = \{r = 0, 0 \leq \theta < \pi/2\}$ and $\mathcal{D}_2 = \{r = 0, \pi/2 < \theta \leq \pi\}$. The coordinate regions of the maximal analytic continuation of the Riemann surface \mathcal{V} of the magic potential in extended oblate spheroidal coordinates are listed in Table 3.

Topology of the Riemann Surface \mathcal{V}		
Sheet 1	\mathcal{V}_1	$\mathcal{V}_1^+ = \{r \geq 0, 0 \leq \theta \leq \pi/2\}$ $\mathcal{V}_1^- = \{r \geq 0, \pi/2 < \theta \leq \pi\}$
Sheet 2	\mathcal{V}_2	$\mathcal{V}_2^+ = \{r \leq 0, \pi/2 \leq \theta \leq \pi\}$ $\mathcal{V}_2^- = \{r \leq 0, 0 \leq \theta < \pi/2\}$
Gate 1	\mathcal{D}_1	$\mathcal{V}_1^+ \cap \mathcal{V}_2^- = \{r = 0, 0 \leq \theta < \pi/2\}$
Gate 2	\mathcal{D}_2	$\mathcal{V}_1^- \cap \mathcal{V}_2^+ = \{r = 0, \pi/2 < \theta \leq \pi\}$
Ring Singularity	\mathcal{R}	$\partial\mathcal{D}_1 = \partial\mathcal{D}_2 = \{r = 0, \theta = \pi/2\}$

Table 3: Topology of the maximal analytic continuation of the magic potential and the coordinate regions of its constituents. The signs \pm stand for the “upper-half” ($z \geq 0$) and “lower-half” ($z \leq 0$) parts of the sheets. By convention, we have included the gate parts, $r = 0$, in sheet definitions for easy specification of the two gates as intersections of the two sheets.

Under the transformation (2.10), the background metric transforms to

$$ds^2 = \frac{\Sigma}{r^2 + a^2} dr^2 + \Sigma d\theta^2 + (r^2 + a^2) \sin^2 \theta d\phi^2 \quad (2.12)$$

where $\Sigma = r^2 + a^2 \cos^2 \theta$. This is the $m \rightarrow 0$ limit of the Kerr metric and the $G \rightarrow 0$ limit of the Kerr-Newman metric. The metric (2.12) is flat everywhere outside the ring \mathcal{R} . A consequence of the nontrivial topology of the Riemann surface \mathcal{V} is that if we round the ring \mathcal{R} and pass through the disk \mathcal{D} , say in a ϕ -constant plane, we need to go round twice to return to the starting point. For more explanation, see the following discussion and also Figure 4. This 4π angle rounding means that \mathcal{R} is a conical singularity with a 2π angular excess.

The 2π angular excess can be demonstrated by introducing the closed curve γ rounding the ring \mathcal{R} on ϕ -constant plane parameterized by an angle α so that

$$r = \epsilon |a| \sin \frac{\alpha}{2}, \quad \cos \theta = \epsilon \cos \frac{\alpha}{2}. \quad (2.13)$$

For $0 < \alpha < 2\pi$, the curve γ circles the ring in the first sheet \mathcal{V}_1 , and for $2\pi < \alpha < 4\pi$, it circles that in the second sheet \mathcal{V}_2 , cf. Figure 4.

For a small ϵ , the shape of γ tends to become a circle with the circumference as

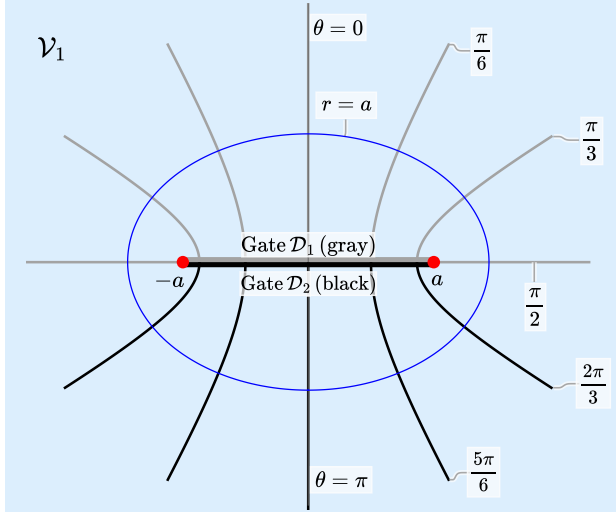
$$\int_0^{4\pi} \sqrt{g(\dot{\gamma}, \dot{\gamma})} d\alpha = 2\pi |a| \epsilon^2 + \mathcal{O}(\epsilon^3) \quad (2.14)$$

and the radius, i.e. the distance from its center on the ring \mathcal{R} , as

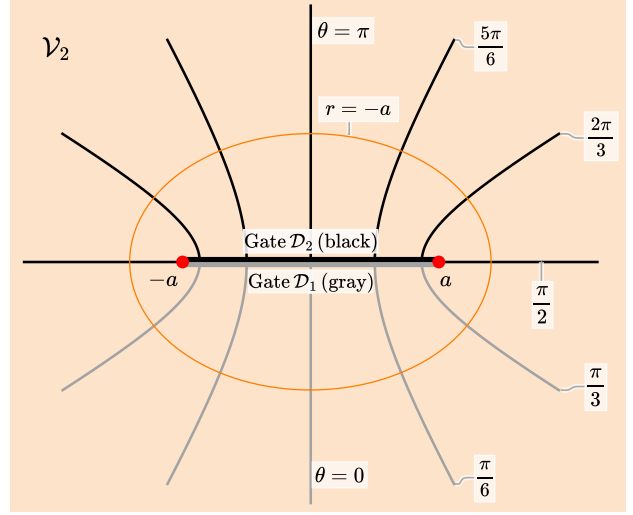
$$\sqrt{(\chi - a)^2 + z^2} = \frac{|a|}{2} \epsilon^2 + \mathcal{O}(\epsilon^3). \quad (2.15)$$

Therefore, the ratio of the circumference to the radius is 4π in the limit that γ shrinks to a point. The same analysis is done in [23] by a slightly different parametrization. We will use the relations (2.13) in introducing a useful coordinate system later.

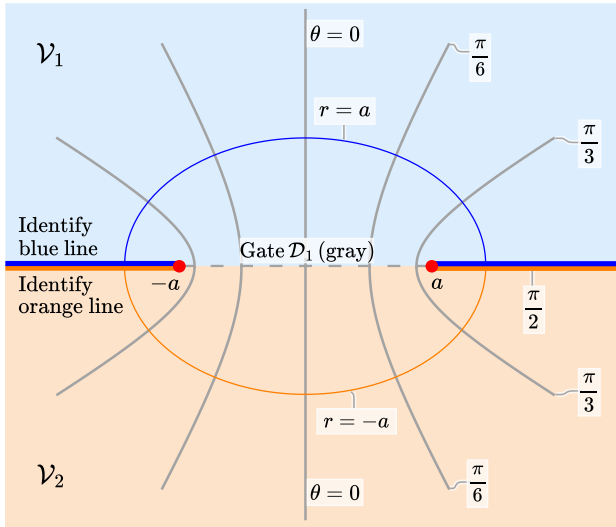
It is noteworthy that by considering the analytic continuation, the apparent discontinuity of the electric and magnetic fields in Figure 2 is no longer present, cf. 5.



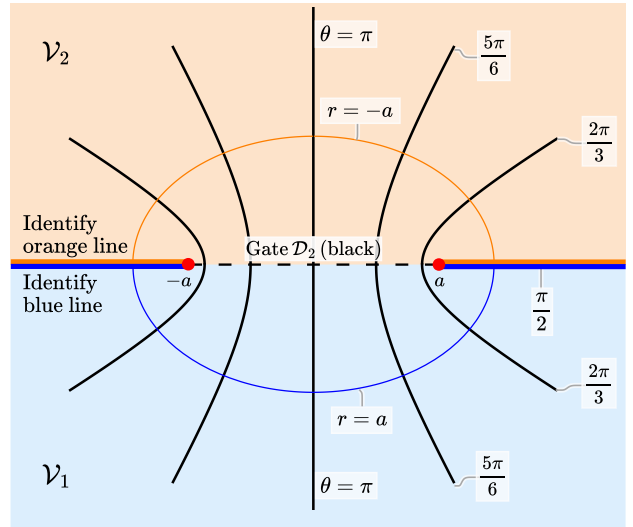
(a) First sheet \mathcal{V}_1



(b) Second sheet \mathcal{V}_2



(c) First gate \mathcal{D}_1



(d) Second gate \mathcal{D}_2

Figure 3: The whole Riemann surface \mathcal{V} of the electromagnetic magic field: (a) the first sheet \mathcal{V}_1 , (b) the second sheet \mathcal{V}_2 , (c) the first gate \mathcal{D}_1 between the upper part of the first sheet \mathcal{V}_1^+ and the lower part of the second sheet \mathcal{V}_2^- , and (d) the second gate \mathcal{D}_2 between the lower part of first sheet \mathcal{V}_1^- and the upper part of the second sheet \mathcal{V}_2^+ . The red points represent the ring singularity \mathcal{R} . The blue and orange line segments that separate the upper and lower halves in (c) and (d) are identified respectively.

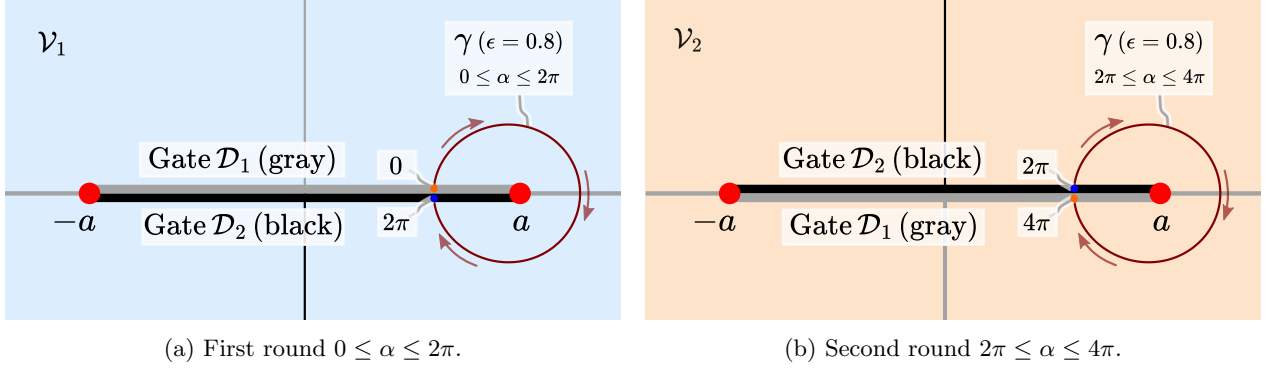


Figure 4: Curve γ circling around the ring singularity \mathcal{R} in double-sheeted Riemann surface \mathcal{V} . For $0 \leq \alpha \leq 2\pi$, the curve γ is in the first sheet \mathcal{V}_1 starting from the orange point $\alpha = 0$. It enters the second sheet \mathcal{V}_2 from the black gate \mathcal{D}_2 at $\alpha = 2\pi$ depicted by the blue point on the gate. For $2\pi \leq \alpha \leq 4\pi$, it is in the second sheet \mathcal{V}_2 and enters back to the first sheet from the gray gate \mathcal{D}_1 and closes at the starting point. The depicted curve is an ϵ -constant curve, ϵ being the semi-radius of the curve defined in (2.13).

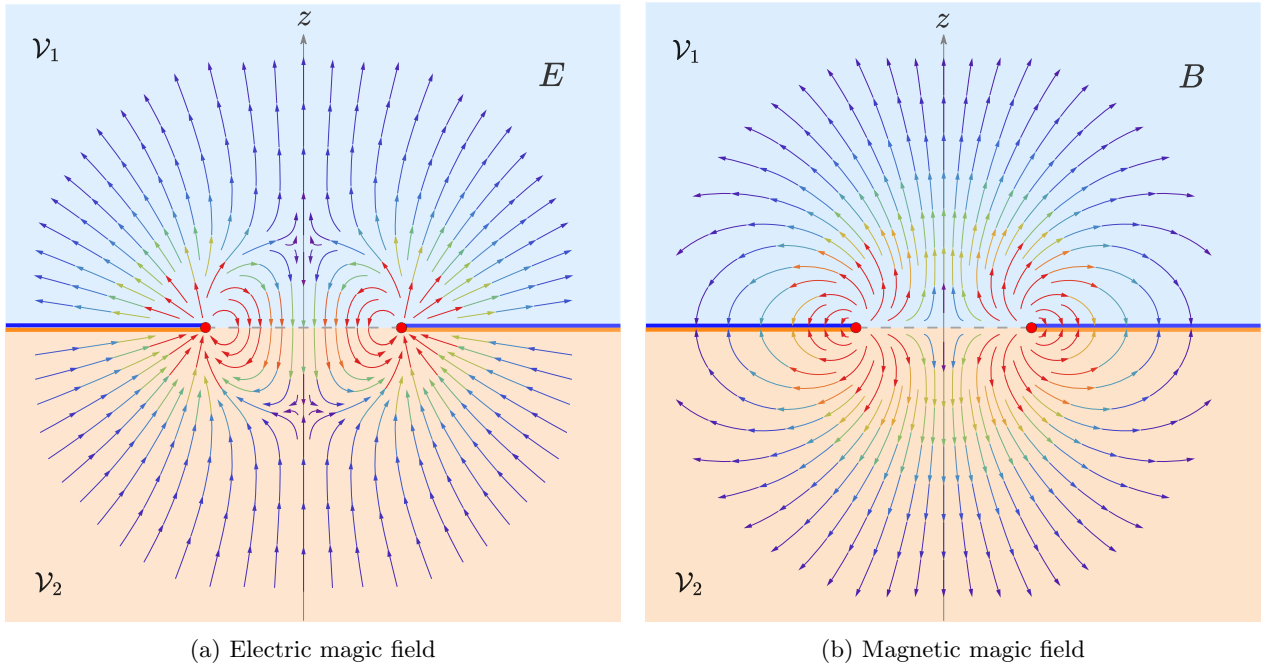


Figure 5: Electric and magnetic components of the magic field through the gate \mathcal{D}_1 of the Riemann surface \mathcal{V} of the complex potential. The rainbow color-coding demonstrates the fields strengths, with red representing the extreme values and purple the negligible ones. The red points on the χ -axis display the singular ring \mathcal{R} intersections, and the line segment between them displays the intersection of the branch-cut disk \mathcal{D} spanned by the ring \mathcal{R} . The fields have azimuthal symmetry around the z -axis. There is no discontinuity of the field on the disk spanned by the singular ring. Similar graphs can show the fields structure in the other gate \mathcal{D}_2 .

2.2 Self-energy and Lagrangian of a Magic Field

In this section, we analyze the free Electromagnetic Lagrangian for a single magic field in its nontrivial two-sheeted background topology. To this end, we exploit the stationarity of the magic field to write the electromagnetic Lagrangian integral over the spatial space as a surface integral using Stokes' theorem. The method developed here will be applied to our analysis of interaction Lagrangian of the magic fields in the following sections.

Electromagnetic Lagrangian Let \mathcal{V} be a spatial leaf (i.e. a Cauchy time slice) of the spacetime manifold \mathcal{M} . The total (free) electromagnetic Lagrangian, in terms of the Weber-Silberstein vector (2.1) can be written as

$$L = \frac{1}{2\Omega} \int_{\mathcal{V}} (\mathbf{E}^2 - \mathbf{B}^2) dV = \text{Re}[\mathcal{L}] , \quad (2.16)$$

where \mathcal{L} is the complex Lagrangian⁶ defined as

$$\mathcal{L} := \frac{1}{2\Omega} \int_{\mathcal{V}} \mathcal{F}^2 dV . \quad (2.17)$$

In the above expressions dV is the volume element on the spatial leaf \mathcal{V} , and Ω is the solid angle of the whole spatial infinity of the asymptotic region of \mathcal{V} . In usual cases, where \mathcal{V} is one-sheeted, $\Omega = 4\pi$. However, in the case of the magic field, where the background is two-sheeted, we have $\Omega = 8\pi$. Although it is unnecessary to specify the value of Ω for the analysis in this section, we will see later that it becomes important to recover the Coulomb limit of the interaction consistently.

Using the potential representation for stationary solutions (2.3), the complex Lagrangian (2.17) is recast in

$$\begin{aligned} \mathcal{L} &= \frac{1}{2\Omega} \int_{\mathcal{V}} \mathcal{F}^2 dV = \frac{1}{2\Omega} \int_{\mathcal{V}} \nabla \mathcal{Z} \cdot \nabla \mathcal{Z} dV \\ &= \frac{1}{2\Omega} \int_{\mathcal{V}} [\nabla \cdot (\mathcal{Z} \nabla \mathcal{Z}) - \mathcal{Z} \nabla^2 \mathcal{Z}] dV \\ &= \frac{1}{4\Omega} \oint_{\partial\mathcal{V}} \nabla \mathcal{Z}^2 \cdot d\mathbf{S} , \end{aligned} \quad (2.18)$$

where $d\mathbf{S}$ is the directed area element of the boundary $\partial\mathcal{V}$ toward outside, and for the last equality, we have used Stokes' theorem and used (2.4) on \mathcal{V} .

Lagrangian of a single magic field To analyze the Lagrangian (2.18) for a single magic field on its Riemann surface \mathcal{V} , we need to locate the boundary $\partial\mathcal{V}$. The outer boundary consists of two distinct asymptotic regions, where the value of the potential and field tends rapidly enough to zero. The inner boundary is a double torus that surrounds the ring singularity from both sheets. We can describe this surface by the limit of a level surface of Σ , when its value tends to zero. If we use the equations (2.13) to introduce a new coordinate system (ϵ, α, ϕ) as

$$r = \epsilon |a| \sin \frac{\alpha}{2} , \quad \cos \theta = \epsilon \cos \frac{\alpha}{2} , \quad \phi = \phi . \quad (2.19)$$

In this coordinate system, we have

$$\Sigma = r^2 + a^2 \cos^2 \theta = a^2 \epsilon^2 . \quad (2.20)$$

The non-orthonormal basis vectors in this coordinate system consist of

$$\partial_{\epsilon} = \frac{r}{\epsilon} \partial_r - \frac{\cot \theta}{\epsilon} \partial_{\theta} \quad (2.21)$$

$$\partial_{\alpha} = \frac{|a|}{2} \cos \theta \partial_r + \frac{r}{2|a|} \csc \theta \partial_{\theta} \quad (2.22)$$

⁶We always use this complex Lagrangian throughout the text, and the standard Lagrangian is just the real part of it, see Eq. (2.16).

and $\boldsymbol{\partial}_\phi$. The (outward) unit normal vector to the surface reads

$$\mathbf{n} = \frac{\sqrt{1 - \epsilon^2 \cos \alpha}}{|a| \epsilon} \boldsymbol{\partial}_\epsilon + \frac{\sin \alpha}{|a| \sqrt{1 - \epsilon^2 \cos \alpha}} \boldsymbol{\partial}_\alpha . \quad (2.23)$$

Using (α, ϕ) parameterization of a ϵ -constant surface, the (outward) vectorial area element can be written in terms of the tangent vectors $\boldsymbol{\partial}_\alpha$ and $\boldsymbol{\partial}_\phi$ as

$$(\mathrm{d}\mathbf{S})^i = \sqrt{g} \varepsilon^i{}_{jk} (\boldsymbol{\partial}_\alpha)^j (\boldsymbol{\partial}_\phi)^k \mathrm{d}\alpha \mathrm{d}\phi , \quad (2.24)$$

where $\sqrt{g} = |a|^3 \epsilon^3 / 2$ and ε_{ijk} is the Levi-Civita symbol in new coordinates⁷

The Lagrangian of the magic field on its Riemann surface \mathcal{V} is obtained as

$$\begin{aligned} \mathcal{L} &= \frac{1}{4\Omega} \oint_{\partial\mathcal{V}} \nabla \mathcal{Z}^2 \cdot \mathrm{d}\mathbf{S} \\ &= \frac{1}{32\pi} \int_0^{2\pi} \mathrm{d}\phi \int_0^{4\pi} \mathrm{d}\alpha \frac{q^2}{4|a|} (1 + 3e^{-2i\alpha} - 4\epsilon^{-2} e^{-i\alpha}) \\ &= \frac{\pi q^2}{16|a|} . \end{aligned} \quad (2.25)$$

Note that here, the integral over the outer boundary at infinity vanishes, and the volume form on the inner toroidal surface is inward, thus a minus sign with respect to (2.24). The value of Lagrangian for the magic field given by (2.25) is therefore finite for a finite spin parameter a and diverges in the Coulomb limit $a \rightarrow 0$ as expected. In the same manner, we can calculate the self-energy, which is obtained as

$$\begin{aligned} \mathcal{E} &= \frac{1}{4\Omega} \oint_{\partial\mathcal{V}} \nabla (\mathcal{Z} \mathcal{Z}^*) \cdot \mathrm{d}\mathbf{S} \\ &= \lim_{\epsilon \rightarrow 0} \frac{q^2}{16|a|\epsilon^2} , \end{aligned} \quad (2.26)$$

which diverges, as is the case for the Coulomb field.

3 Interaction of Two Magic Fields

In this section, we study the interaction of two electromagnetic magic fields. We calculate the interaction Lagrangian for two Coulomb fields, as well as for two electromagnetic magic fields in two cases: first, in an up-down configuration when their symmetry axis coincides, and second, in a side-by-side configuration when their ring singularities are laid in the same plane. We will discuss the topology of the superposition of magic fields in these configurations.

Since Maxwell's equations (2.2) are linear equations, the superposition of two electromagnetic fields $\mathcal{F}_{\mathrm{tot}} = \mathcal{F}_1 + \mathcal{F}_2$ is a solution of those equations if its ingredients are so. For such a superposition, the total (complex) Lagrangian (2.17) is recast into

$$\mathcal{L}_{\mathrm{tot}} = \mathcal{L}_1 + \mathcal{L}_2 + \mathcal{L}_{\mathrm{int}} , \quad (3.1)$$

with definitions of (complex) *self-Lagrangians* as

$$\mathcal{L}_n = \frac{1}{2\Omega} \int_{\mathcal{V}} \mathcal{F}_n^2 \mathrm{d}V \quad , \quad n = 1, 2 , \quad (3.2)$$

for either of the fields⁸, and the (complex) *interaction Lagrangian* as

$$\mathcal{L}_{\mathrm{int}} = \frac{1}{\Omega} \int_{\mathcal{V}} \mathcal{F}_1 \cdot \mathcal{F}_2 \mathrm{d}V . \quad (3.3)$$

In the static case, where the kinetic term is absent, the interaction Lagrangian can be viewed as defining an interaction potential.

⁷We can equivalently find the area element as $\mathrm{d}\mathbf{S} = \sqrt{h} \mathbf{n}$, with h being the determinant of the induced metric on the toroidal Σ -surface, which leads to the same result.

⁸In the Coulomb case, the self-Lagrangian diverges, while for the magic field, the integral is convergent; see (2.25).

For stationary solutions $\mathcal{F}_1 = -\nabla\mathcal{Z}_1$ and $\mathcal{F}_2 = -\nabla\mathcal{Z}_2$, the interaction Lagrangian (3.3) is

$$\begin{aligned}\mathcal{L}_{\text{int}} &= \frac{1}{\Omega} \int_{\mathcal{V}} \nabla\mathcal{Z}_1 \cdot \nabla\mathcal{Z}_2 \, dV \\ &= \frac{1}{2\Omega} \int_{\mathcal{V}} [\nabla \cdot (\mathcal{Z}_1 \nabla\mathcal{Z}_2 + \mathcal{Z}_2 \nabla\mathcal{Z}_1) - \mathcal{Z}_1 \nabla^2\mathcal{Z}_2 - \mathcal{Z}_2 \nabla^2\mathcal{Z}_1] \, dV \\ &= \frac{1}{2\Omega} \oint_{\partial\mathcal{V}} \nabla(\mathcal{Z}_1\mathcal{Z}_2) \cdot d\mathbf{S}\end{aligned}\tag{3.4}$$

where \mathcal{V} is the Riemann surface of \mathcal{F}_{tot} and the last equality holds when the divergence terms vanish inside \mathcal{V} and we take the limit toward the singular regions for the boundary $\partial\mathcal{V}$.

For the superposition of two Coulomb fields, the self-Lagrangians \mathcal{L}_1 and \mathcal{L}_2 in (3.1) diverge. However, the interaction Lagrangian (3.3) is still well-defined and can be evaluated as follows. Consider two point charges located at $z = \pm z_0$

$$\mathcal{Z}_{\pm} = \frac{q_{\pm}}{\sqrt{\chi^2 + (z \mp z_0)^2}},\tag{3.5}$$

where $\chi^2 = x^2 + y^2$. The spatial leaf \mathcal{V} , over which we calculate the interaction Lagrangian, is the three-dimensional Euclidean space without two points at $z = \pm z_0$ on the z -axis: $\mathcal{V} = \mathbb{R}^3 - \{(0, 0, \pm z_0)\}$ and $\Omega = 4\pi$. The interaction Lagrangian in (3.4) has three sectors: two inner ones, each around either of the point singularities, and an outer one at infinity. The latter vanishes due to the fall-off behavior of the fields. To evaluate the surface integrals over the inner boundaries, we consider those boundaries to be two cylindrical pill-boxes \mathcal{P}_{\pm} around the point singularities. The calculation is straightforward, and the results of the two integrations add up to

$$\begin{aligned}\mathcal{L}_{\text{int}} &= \frac{1}{8\pi} \left(\oint_{\mathcal{P}_+} \nabla(\mathcal{Z}_+ \mathcal{Z}_-) \cdot d\mathbf{S} + \oint_{\mathcal{P}_-} \nabla(\mathcal{Z}_+ \mathcal{Z}_-) \cdot d\mathbf{S} \right) \\ &= (q_+ q_-) \frac{1}{d},\end{aligned}\tag{3.6}$$

which is, as expected, proportional to the inverse of the distance $d = 2z_0$ of the field singular points.

As for the interacting magic fields, we need to analyze the topology of the Riemann surface \mathcal{V} of the superposition \mathcal{F}_{tot} . Recall that a single magic field's potential \mathcal{Z} is continuous and single-valued on a two-sheeted extended space. In the case of interacting magic fields, each of the potentials⁹, \mathcal{Z}_+ and \mathcal{Z}_- , can be in one of two branch configurations on a given sheet. Therefore, the superposed potential $\mathcal{Z}_{\text{tot}} = \mathcal{Z}_+ + \mathcal{Z}_-$ is continuous on a Riemann surface consisting of four sheets. Figure 6 shows the topology of the entire Riemann surface of two interacting magic fields and a curve that initiates from one sheet, passes through the gates to all other sheets, and returns back to the beginning point.

The interaction Lagrangian (3.4) consists of surface integrals over the boundaries $\partial\mathcal{V}$ of the four-sheeted Riemann surface \mathcal{V} . However, the complex function $\mathcal{Z}_+ \mathcal{Z}_-$ has only two branches and has different overall signs in two pairs of equivalent sheets as written in Figure 6. These signs cancel the sign change due to the change of orientation of the coordinate system, and therefore, the integrals have the same value on all sheets. Moreover, in this case, instead of tube-like surfaces that cover the ring singularities in both sheets, integrating over two closed infinitesimal surfaces \mathcal{P}_{\pm} around each singularity in either of the sheets yields the same result. Taking the overall factor in (3.3) yields $4 \times 1/2\Omega = 1/8\pi$ into account, the interaction Lagrangian takes a similar form to the Coulomb case as

$$\mathcal{L}_{\text{int}} = \frac{1}{8\pi} \left(\oint_{\mathcal{P}_+} \nabla(\mathcal{Z}_+ \mathcal{Z}_-) \cdot d\mathbf{S} + \oint_{\mathcal{P}_-} \nabla(\mathcal{Z}_+ \mathcal{Z}_-) \cdot d\mathbf{S} \right).\tag{3.7}$$

We evaluate this in two different arrangements, with the ring singularities located in up-down and side-by-side configurations.

⁹The sign indices \pm of potential \mathcal{Z}_{\pm} in this general consideration only refer to either of the interacting fields, but in the subsequent sections, they refer to upper/lower or right/left position of the field singularities, respectively.

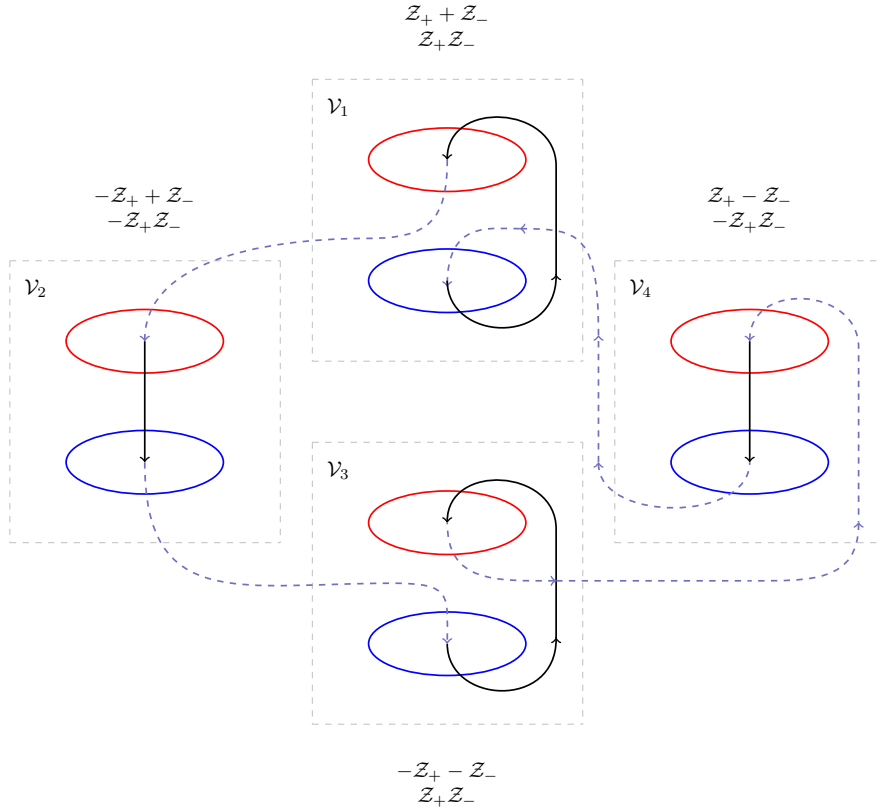


Figure 6: Topological structure of the Riemann surface of two interacting Magic Fields. Each gray dashed square is a distinct sheet. A curve (solid line) passes through the gates (disks) and goes from one sheet to another. Dashed lines demonstrate such passing. The branch of the potentials at each sheet is indicated by the relative sign with respect to the principal branch for both superposition and product.

3.1 Interaction of Magic Fields in Up-down Configuration

In this section, we study the interaction of two electromagnetic magic fields in an up-down configuration. Consider two electromagnetic magic fields, with their ring singularities on $z = \pm z_0$ and oriented along the z -axis with potentials

$$\mathcal{Z}_{\pm} = \frac{q_{\pm}}{\sqrt{\chi^2 + (z \mp z_0 - i a_{\pm})^2}}, \quad (3.8)$$

where the plus and minus signs refer to the upper and lower rings, which have, in general, different electric charges q_{\pm} and spin parameters a_{\pm} .

We evaluate the surface integrals in (3.7) on two cylindrical pillboxes \mathcal{P}_{\pm} , around the two ring singularities, as shown in Figure 7. The azimuthal symmetry of the problem in integrands and surfaces allows us to exploit the polar coordinates (χ, ϕ, z) to expand the involving integrals as

$$\oint_{\mathcal{P}_{\pm}} \nabla(\mathcal{Z}_+ \mathcal{Z}_-) \cdot d\mathbf{S} = - \int_{\mathcal{D}_{\pm}^+} \frac{\partial}{\partial z}(\mathcal{Z}_+ \mathcal{Z}_-) dS + \int_{\mathcal{D}_{\pm}^-} \frac{\partial}{\partial z}(\mathcal{Z}_+ \mathcal{Z}_-) dS \quad (3.9)$$

where $dS = \chi d\chi d\phi$ is the area element on upper \mathcal{D}_{\pm}^+ and lower \mathcal{D}_{\pm}^- disk-like bases of the upper pillbox \mathcal{P}_+ (and similarly, bases \mathcal{D}_{\pm}^{\pm} of the lower pillbox \mathcal{P}_-) in polar coordinates, while the vanishing parts of the integrals over the cylindrical sides of the pillboxes are eliminated. The signs of each term in (3.9) are produced by the direction of the normals of the surfaces, which are toward inside the pillboxes.

The pillboxes \mathcal{P}_{\pm} are infinitesimal surfaces, and we have to take the appropriate limits so that their heights tend to zero and the radius of each of them tends to the radius of the covered ring singularity from outside. The order of integration, adding up the contributions for each pillbox, and taking the limits are important in this computation. This is because the limiting process makes the phase of $\mathcal{Z}_+ \mathcal{Z}_-$ ambiguous during the integration. In other words, taking the limit before integration leads to incorrect results.

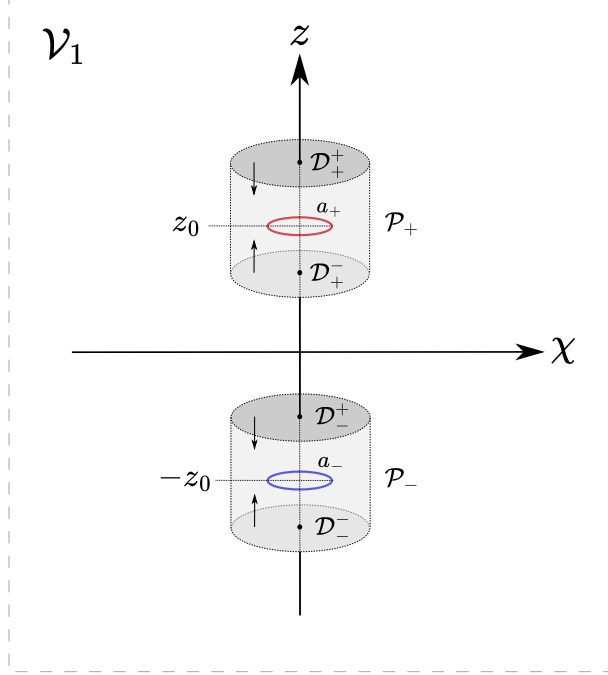


Figure 7: Up-down magic field configuration

The integrals in the right-hand sides of equations (3.9) over all four disks \mathcal{D}_{\pm}^{\pm} are of the same form, and we can calculate them by using the primitive integral

$$\begin{aligned}
 F(\chi, z) &:= \int \frac{\partial}{\partial z} \left(\frac{1}{\sqrt{\chi^2 + A_+(z)} \sqrt{\chi^2 + A_-(z)}} \right) \chi d\chi \\
 &= \frac{1}{2(A_+ - A_-)} \left(-A'_+ \frac{\sqrt{\chi^2 + A_-}}{\sqrt{\chi^2 + A_+}} + A'_- \frac{\sqrt{\chi^2 + A_+}}{\sqrt{\chi^2 + A_-}} \right) + c
 \end{aligned} \tag{3.10}$$

and substitutions

$$A_{\pm}(z) = (z \mp z_0 - i a_{\pm})^2, \quad A'_{\pm}(z) = 2(z \mp z_0 - i a_{\pm}). \tag{3.11}$$

Using this relation and substitutions and specifying the proper limits for infinitesimal disks \mathcal{D}_{\pm}^{\pm} , we obtain the right-hand side of (3.9) as

$$\oint_{\mathcal{P}_{\pm}} \nabla(\mathcal{Z}_+ \mathcal{Z}_-) \cdot d\mathbf{S} = 2\pi q_+ q_- \times \lim_{a \rightarrow |a_{\pm}|} \left[- \lim_{z \rightarrow \pm z_0^+} F(\chi, z) \Big|_{\chi=0}^{\chi=a} + \lim_{z \rightarrow \pm z_0^-} F(\chi, z) \Big|_{\chi=0}^{\chi=a} \right], \tag{3.12}$$

where the factor of 2π is the result of integration over azimuthal angular coordinate ϕ . Note that the order of the limits is crucial in this calculation, as we will see in the following.

In order to proceed further and find the values of the terms in (3.12), we need to analyze the square root functions in (3.10) with (3.11), and consistently choose the branches for them. To be more specific, consider the square root function $\sqrt{\chi^2 + A_+}$, with A_+ in (3.11), that is in fact the inverse of the potential \mathcal{Z}_+ . This function vanishes on the upper ring singularity ($\chi = |a_+|, z = z_0$). Around this ring, i.e. over the upper/lower base \mathcal{D}_{\pm}^{\pm} of the upper pillbox \mathcal{P}_+ , we need to analyze the limits

$$\sqrt{\chi^2 + A_+} \Big|_{\mathcal{D}_{\pm}^{\pm}} = \lim_{z \rightarrow z_0^{\pm}} \sqrt{\chi^2 + (z - z_0 - i a_+)^2} = \lim_{\epsilon \rightarrow 0^{\pm}} \sqrt{\chi^2 + (\epsilon - i a_+)^2}. \tag{3.13}$$

The argument of the radicant of this function is in the intervals

$$\arg(\chi^2 + A_+) \in \begin{cases} (-\pi, 0) & \text{over upper disk } \mathcal{D}_+^+, \\ (0, \pi) & \text{over lower disk } \mathcal{D}_+^-, \end{cases} \tag{3.14}$$

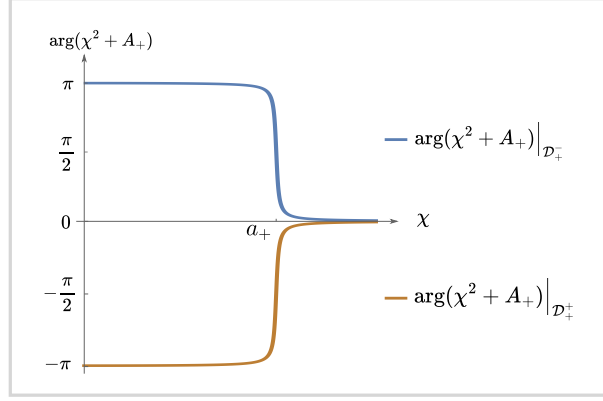


Figure 8: Argument of the radicand of $\sqrt{\chi^2 + A_+}$, with $A_+ = (\epsilon - i a_+)^2$ for infinitesimal $\epsilon \rightarrow 0^\pm$ over the disk \mathcal{D}_+^\pm .

and its behaviour is depicted in figure 8.

Using the principal branch cut at $\arg(\alpha) = \pm\pi$, i.e. the negative real axis, we can compute the contributions from each limit in (3.12). In particular, at the upper limit of integrals at $\chi = a > |a_+|$, we have

$$\lim_{\epsilon \rightarrow 0^\pm} \sqrt{\chi^2 + (\epsilon - i a_+)^2} \Big|_{\chi=a} = \sqrt{a^2 - a_+^2} > 0, \quad (3.15)$$

regardless of the disk. Since other ingredients of the function $F(\chi, z)$ have the same finite value on \mathcal{D}_+^\pm , the two terms in (3.12), due to their different signs, cancel out at this limit. Therefore, the limit $a \rightarrow a_+$ yields no divergence but vanishes smoothly.

On the other hand, at the lower limit $\chi = 0$, we have

$$\lim_{\epsilon \rightarrow 0^\pm} \sqrt{\chi^2 + (\epsilon - i a_+)^2} \Big|_{\chi=0} = \mp i a_+. \quad (3.16)$$

Therefore, at this limit, we can explicitly derive

$$\begin{aligned} & \lim_{z \rightarrow z_0^+} F(\chi, z) \Big|_{\chi=0} \\ &= \lim_{\epsilon \rightarrow 0^+} \frac{1}{(\epsilon - i a_+)^2 - (2z_0 - i a_-)^2} \left[-(\epsilon - i a_+) \frac{\sqrt{(2z_0 - i a_-)^2}}{\sqrt{(\epsilon - i a_+)^2}} + (2z_0 - i a_-) \frac{\sqrt{(\epsilon - i a_+)^2}}{\sqrt{(2z_0 - i a_-)^2}} \right] \\ &= \frac{1}{(i a_+)^2 - (2z_0 - i a_-)^2} \left[-\sqrt{(2z_0 - i a_-)^2} + (2z_0 - i a_-) \frac{-i a_+}{\sqrt{(2z_0 - i a_-)^2}} \right] \\ &= \frac{1}{2z_0 - i(a_+ + a_-)}, \end{aligned} \quad (3.17)$$

where for the last equal, we have used $z_0 > 0$, and thus $\sqrt{(2z_0 - i a_-)^2} = 2z_0 - i a_-$. Now due to the signs of the terms in (3.12) and additional signs from (3.16), the contributions of the lower and upper disks \mathcal{D}_+^\pm are equal, and therefore for the upper pillbox \mathcal{P}_+ , we have

$$\begin{aligned} \oint_{\mathcal{P}_+} \nabla(\mathcal{Z}_+ \mathcal{Z}_-) \cdot d\mathbf{S} &= 4\pi q_+ q_- \times \lim_{z \rightarrow z_0^+} F(\chi^2, z) \Big|_{\chi=0} \\ &= \frac{4\pi q_+ q_-}{2z_0 - i(a_+ + a_-)}, \end{aligned} \quad (3.18)$$

Similar analysis can be carried out for the other singularity-generating square root function $\sqrt{\chi^2 + A_-}$ on the surfaces around the lower singularity at $(\chi = |a_-|, z = -z_0)$. We can employ the transformation $(a_+ \leftrightarrow a_- \text{ and } z_0 \leftrightarrow -z_0)$, relating the upper and lower potential functions \mathcal{Z}_\pm in (3.8) and also in (3.11), to transform the result found in (3.18) for the upper pillbox \mathcal{P}_+ to the result of integration on the lower

pillbox \mathcal{P}_- . To do so, we must apply this transformation before simplifying the square roots. In particular in transforming (3.17), we encounter $\sqrt{(-2z_0 - ia_+)^2} = 2z_0 + ia_+$, which produces an extra overall minus sign. Performing this computation yields

$$\begin{aligned} \oint_{\mathcal{P}_-} \nabla(\mathcal{Z}_+ \mathcal{Z}_-) \cdot d\mathbf{S} &= 4\pi q_+ q_- \times \lim_{z \rightarrow -z_0^+} F(\chi^2, z) \Big|_{\chi=0} \\ &= \frac{4\pi q_+ q_-}{2z_0 + i(a_+ + a_-)}, \end{aligned} \quad (3.19)$$

which is the transformed (3.18) with an extra overall minus sign.

Finally, the total interaction Lagrangian (3.7) for two magic fields in up-down positions is obtained as

$$\begin{aligned} \mathcal{L}_{\text{int}} &= \frac{1}{8\pi} \left(\frac{4\pi q_+ q_-}{2z_0 - i(a_+ + a_-)} - \frac{4\pi q_+ q_-}{2z_0 + i(a_+ + a_-)} \right) \\ &= (q_+ q_-) \frac{d}{d^2 + (a_+ + a_-)^2} \end{aligned} \quad (3.20)$$

where $d = 2z_0$ is the distance between the centers of the singularity rings. Notice that the total interaction Lagrangian is real and, in the spin-zero limit, reproduces the Coulomb interaction. Since we haven't restricted the signs of a_{\pm} throughout the calculation, they can represent both aligned and anti-aligned spins.

3.2 Interaction of Magic Fields in Side-by-side Configuration

In this section, we study the interaction of two electromagnetic magic fields in a side-by-side configuration. Consider two magic fields whose ring singularities are located on a plane with their centers at $x = \pm x_0$ separated by a distance $d = 2x_0$, see figure 9.

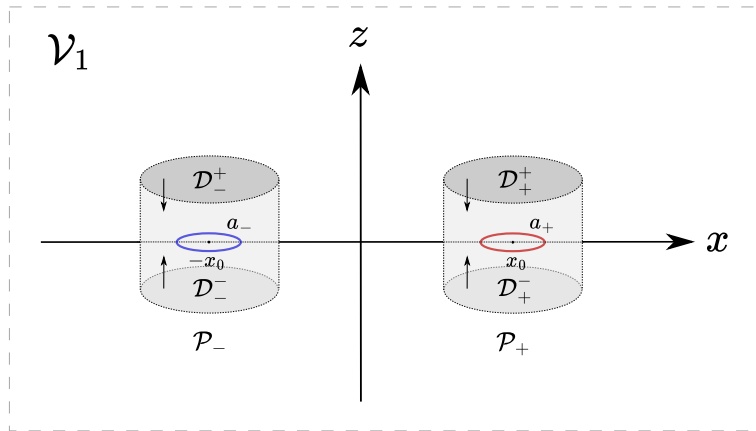


Figure 9: Side-by-side magic field configuration

Like the previous section, the magic fields have, in general, different spin parameters, i.e. ring radii $a_+ \neq a_-$. In Cartesian coordinates (x, y, z) , complex scalar potentials for magic fields are

$$\mathcal{Z}_{\pm} = \frac{q_{\pm}}{\sqrt{(x \mp x_0)^2 + y^2 + (z - ia_{\pm})^2}}, \quad (3.21)$$

The topology of the superposition field is the same as what we analyzed before and depicted in Figure 6. The only difference is that the ring singularities are positioned side by side in each sheet. The interaction Lagrangian, therefore, has the same form as (3.7) with \mathcal{P}_{\pm} being the pair of left and right infinitesimal pillboxes in either of the sheets. This configuration has no azimuthal symmetry, and we need to introduce an adapted coordinate system to evaluate the integrals. However, we can expand the involving integrals in Cartesian coordinates over the bases of the pill-boxes as

$$\oint_{\mathcal{P}_{\pm}} \nabla(\mathcal{Z}_+ \mathcal{Z}_-) \cdot d\mathbf{S} = - \int_{\mathcal{D}_{\pm}^+} \frac{\partial}{\partial z}(\mathcal{Z}_+ \mathcal{Z}_-) dS + \int_{\mathcal{D}_{\pm}^-} \frac{\partial}{\partial z}(\mathcal{Z}_+ \mathcal{Z}_-) dS \quad (3.22)$$

where $dS = dx dy$ is the area element on upper \mathcal{D}_+^+ and lower \mathcal{D}_+^- disk-like bases of the right pillbox \mathcal{P}_+ (and similarly, bases \mathcal{D}_\pm^\pm of the left pillbox \mathcal{P}_-) in Cartesian coordinates, while the vanishing parts of the integrals over the cylindrical sides of the pillboxes are eliminated. The signs of each term in (3.22) are produced by the direction of the normals of the surfaces, which are toward inside the pillboxes. Each of the integrals has the form

$$G(x, y, z) := \int \frac{\partial}{\partial z} \left(\frac{1}{\sqrt{(x-x_0)^2 + y^2 - \hat{a}_+^2} \sqrt{(x+x_0)^2 + y^2 - \hat{a}_-^2}} \right) dx dy \quad (3.23)$$

where \hat{a}_\pm are complex functions of z as

$$\hat{a}_\pm = a_\pm - iz . \quad (3.24)$$

The attempt to work out the integral (3.23) in Cartesian coordinates leads to elliptic functions, and the analysis gets even more complicated. We adopt another approach, which consists of a coordinate transformation. The symmetries of the configuration would fit the bi-cylindrical coordinates if \hat{a}_\pm were real. Indeed, this is the case in the limit $z \rightarrow 0$, but we need first to integrate and then take this limit from different directions, i.e. above and below the $z = 0$ plane, to find the correct contributions of the disks above and below the singular rings. A reliable approach would be to expand the integrand around $z = 0$, analyze the integrals, and take the limits afterward. Following this approach, we will have over each disk \mathcal{D}_\pm^\pm an expansion like

$$G(x, y, z) = G^0(x, y) + \mathcal{O}(z) , \quad (3.25)$$

where $G^0(x, y)$ are real functions. This allows us to analyze the branches of the square roots and determine the signs before integration, which requires a coordinate transformation.

To determine the correct signs at each disk, we should notice that inside each of the rings, the real part of the corresponding radiant for $z \ll 1$ is negative

$$(x \mp x_0)^2 + y^2 - a_\pm^2 + z^2 < 0 . \quad (3.26)$$

This leads to different signs for that square root on the upper and lower disks. On the contrary, the real part is positive for the points outside the ring, leading to the same sign for the square root on the above and below disks. As a result, considering their different signs in (3.22), the integrals over the disks below and above the same ring singularity, at the integration limit inside the ring, will add up, while at the other limit outside the ring, i.e. the outer boundary of the disk, they will cancel out as z goes to zero. Done with the branch cut analysis, we can further evaluate the real integral G^0 by transforming Cartesian coordinates to bi-polar coordinates.

In the following, we implement a more elegant approach without performing the expansion (3.25), keeping the complex nature of the integrand and applying a complex coordinate transformation.

Performing the derivative with respect to z in (3.23), by the Leibniz rule we get two terms

$$G(x, y, z) = G_+(x, y, z) + G_-(x, y, z) \quad (3.27)$$

where $G_\pm(x, y, z)$ are

$$G_\pm(x, y, z) = \int \frac{i \hat{a}_\pm dx dy}{\left((x \mp x_0)^2 + y^2 - \hat{a}_\pm^2 \right)^{3/2} \sqrt{(x \pm x_0)^2 + y^2 - \hat{a}_\pm^2}} . \quad (3.28)$$

We assume that the singular rings do not overlap. It is equivalent to the condition

$$|a_+| + |a_-| < 2x_0 , \quad (3.29)$$

where $2x_0$ is the distance between centers of the singular rings.

It is convenient to compute the integrals in bipolar coordinates. We consider two-dimensional coordinate transformation between (x, y) and (η, σ) in the form

$$x = \hat{f} \frac{\sinh \eta}{\cosh \eta - \cos \sigma} - \hat{e} , \quad (3.30a)$$

$$y = \hat{f} \frac{\sin \sigma}{\cosh \eta - \cos \sigma} , \quad (3.30b)$$

where f and e are parameters of the transformation which depend on z . The area element reads

$$dx dy = \frac{\hat{f}^2}{(\cosh \eta - \cos \sigma)^2} d\rho d\sigma . \quad (3.31)$$

We choose the parameters of the transformation \hat{f} and \hat{e} to be

$$\hat{f} = \frac{1}{2d} \sqrt{d^4 - 2d^2 (\hat{a}_+^2 + \hat{a}_-^2) + (\hat{a}_+^2 - \hat{a}_-^2)^2} , \quad (3.32)$$

$$\hat{e} = \frac{1}{2d} (\hat{a}_+^2 - \hat{a}_-^2) . \quad (3.33)$$

Since incorporating a_{\pm} , these parameters are complex functions of z and are chosen so that on the $z = 0$ plane, they are real, and the singular rings of the magic fields are described by $\eta^{\pm} = \text{const}$, see Figure 10.

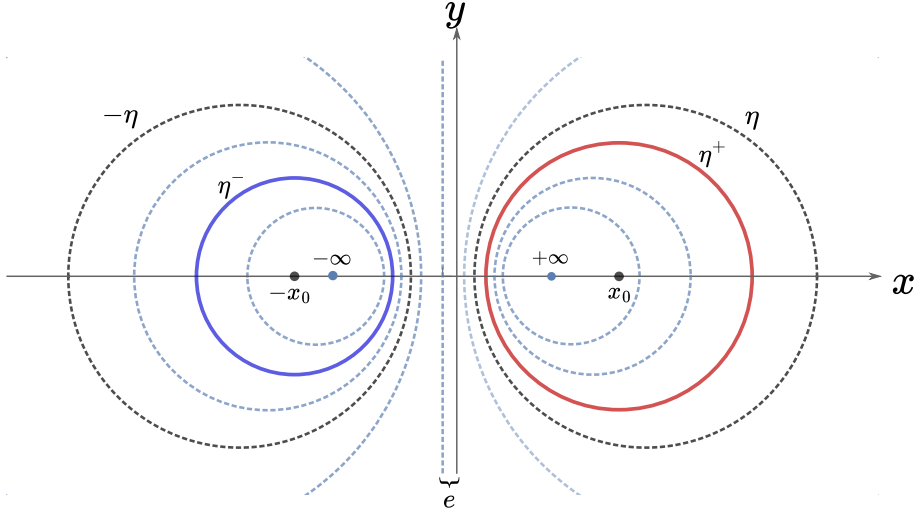


Figure 10: Bi-polar coordinates on $z = 0$ plane: two sets of circles as the level sets of positive and negative values of η , including the ring singularities at η^+ and η^- in red and blue, and the limits of the integral at $\pm\eta$ and $\pm\infty$

The consequence of choosing the transformation parameters to be complex as (3.32) is that the new coordinates (η, σ) are generally complex. In fact, the real (x, y) plane is mapped into a subset of a two-dimensional complex space determined by a set of constraints. The transformation can also be written in the form

$$x + iy = \hat{f} \coth \frac{\eta - i\sigma}{2} - \hat{e} . \quad (3.34)$$

The η -constant loci are circles described by

$$(x - c_\eta)^2 + y^2 = r_\eta^2 , \quad (3.35)$$

with their centers and radii given by

$$c_\eta = \hat{f} \coth \eta + \hat{e} , \quad r_\eta = \frac{\hat{f}}{\sinh \eta} . \quad (3.36)$$

We consider the surfaces \hat{D}_{\pm}^{\pm} consisting of the circles of constant η that intersect with real (x, y) -plane on the x -axis, while the angle σ spans each circle.

Using the transformation (3.30a), we have

$$(x - x_0)^2 + y^2 - \hat{a}_+^2 = \frac{2\hat{f}}{\cosh \eta - \cos \sigma} \left(\hat{f} \cosh \eta - \hat{b}_+ \sinh \eta \right) \quad (3.37)$$

$$(x + x_0)^2 + y^2 - \hat{a}_-^2 = \frac{2\hat{f}}{\cosh \eta - \cos \sigma} \left(\hat{f} \cosh \eta + \hat{b}_- \sinh \eta \right) \quad (3.38)$$

with

$$\hat{b}_{\pm} := \sqrt{\hat{f}^2 + \hat{a}_{\pm}^2} = x_0 \pm \hat{e}. \quad (3.39)$$

As a result, the integrals G_{\pm} in (3.28) transform into

$$\begin{aligned} G_{\pm}(\eta, \sigma, z) &= \frac{1}{4} \int \frac{i \hat{a}_{\pm} \hat{f}^2 d\eta d\sigma}{\left(\hat{f}^2 \cosh \eta \mp \hat{f} \hat{b}_{\pm} \sinh \eta\right)^{3/2} \sqrt{\hat{f}^2 \cosh \eta \pm \hat{f} \hat{b}_{\mp} \sinh \eta}} \\ &= \frac{\pm i \pi \hat{a}_{\pm}}{\hat{f}(\hat{b}_+ + \hat{b}_-)} \frac{\sqrt{\hat{f}^2 \cosh \eta \pm \hat{f} \hat{b}_{\mp} \sinh \eta}}{\sqrt{\hat{f}^2 \cosh \eta \mp \hat{f} \hat{b}_{\pm} \sinh \eta}} \end{aligned} \quad (3.40)$$

The integral on an arbitrary z -plane is to be taken on a complex path for the coordinates (η, σ) , constrained by the reality condition of (x, y) , from a finite value associated with the outer circle, up to the infinity associated with the focal point inside the ring.

$$\begin{aligned} \lim_{z \rightarrow 0^{\pm}} \lim_{\eta \rightarrow +\infty} G_+ &= \frac{i\pi a_+}{2f x_0} \times \frac{\sqrt{f+b_+} \sqrt{f+b_-}}{\mp i a_+} \\ &= \frac{\mp \pi}{2f x_0} \sqrt{(f+x_0)^2 - e^2} \end{aligned} \quad (3.41)$$

$$\begin{aligned} \lim_{z \rightarrow 0^{\pm}} \lim_{\eta \rightarrow +\infty} G_- &= \frac{-i\pi a_-}{2f x_0} \times \frac{\mp i a_+}{\sqrt{f+b_+} \sqrt{f+b_-}} \\ &= \frac{\mp \pi a_+ a_-}{2f x_0} \times \frac{1}{\sqrt{(f+x_0)^2 - e^2}} \end{aligned} \quad (3.42)$$

where the unhatted parameters are the values of z -dependant functions on $z = 0$ plane, which makes all of them to be real. In particular, f and e are

$$f := \hat{f}|_{z=0} = \frac{1}{2d} \sqrt{(d^2 - (a_+ - a_-)^2)(d^2 - (a_+ + a_-)^2)} \quad (3.43)$$

$$e := \hat{e}|_{z=0} = \frac{1}{2d} (a_+^2 - a_-^2) \quad (3.44)$$

Combining these results, we obtain the interaction Lagrangian for two magic fields in a side-by-side position as

$$\begin{aligned} \mathcal{L}_{\text{int}} &= \frac{1}{8\pi} (4\pi q_+ q_-) \frac{d(d+2f) - (a_+ - a_-)^2}{df \sqrt{(d+2f)^2 - 4e^2}} \\ &= (q_+ q_-) \frac{d(d+2f) - (a_+ - a_-)^2}{2df \sqrt{(d+2f)^2 - 4e^2}} \end{aligned} \quad (3.45)$$

where $d = 2x_0$ is the distance between the centers of the singular rings.

3.3 Interaction potential of two magic fields

The interaction potential for two magic fields is obtained from $U = \mathcal{L}_{\text{int}}$. Here, we analyze the interaction potential in two configurations that we calculated in previous sections. For two magic fields in an up-down configuration, the interaction potential is obtained from (3.20) as

$$U_{\text{UD}} = (q_+ q_-) \frac{d}{d^2 + (a_+ + a_-)^2}. \quad (3.46)$$

The form of the interaction potential (3.46) for the up-down configuration was first stated in [29, Eq. (2)], based on heuristic calculations based on a single sheet background that did not take into account the topology of the analytic extension of the magic field.

The potential U_{UD} vanishes in the limit $d \rightarrow 0$ and has extrema at $d = \pm|a_+ + a_-|$ with

$$U_{\text{UD}}^e = \frac{q_+ q_-}{2|a_+ + a_-|}. \quad (3.47)$$

In contrast to the interaction of point particles, the interaction potential contains potential wells that allow for equilibrium points and oscillations. For long-range interactions $a_{\pm} \ll d$, the leading terms are

$$U_{\text{UD}} \approx (q_+ q_-) \left[\frac{1}{d} - \frac{(a_+ + a_-)^2}{d^3} + \mathcal{O}\left(\frac{1}{d^5}\right) \right]. \quad (3.48)$$

In particular, we recover the Coulomb interaction in the spin-zero limit $a_{\pm} \rightarrow 0$. As special cases, we consider the spins of interacting magic fields being either aligned equal $a_{\pm} = a$ as well as anti-aligned equal $a_{\pm} = \pm a$ in up-down configuration. In the aligned case, we obtain

$$U_{\text{UD}} \Big|_{a_{\pm}=a} = (q_+ q_-) \frac{d}{d^2 + 4a^2}, \quad (3.49)$$

whereas in the anti-aligned case, we have

$$U_{\text{UD}} \Big|_{a_{\pm}=\pm a} = (q_+ q_-) \frac{1}{d}. \quad (3.50)$$

The interaction potential in aligned case (3.49) has an extremum at $d = 2|a|$, representing an equilibrium state. The interaction potential in this case is depicted in Figure 11a and 11b for charges having the same or opposite signs, respectively.

For two magic fields in a side-by-side configuration, the interaction potential is obtained from (3.45) as

$$U_{\text{SS}} = (q_+ q_-) \frac{d(d+2f) - (a_+ - a_-)^2}{2df\sqrt{(d+2f)^2 - 4e^2}} \quad (3.51)$$

For long-range interactions $a_{\pm} \ll d$, the leading terms are

$$U_{\text{SS}} \approx (q_+ q_-) \left[\frac{1}{d} + \frac{(a_+ + a_-)^2}{2d^3} + \mathcal{O}\left(\frac{1}{d^5}\right) \right]. \quad (3.52)$$

In particular, we recover the Coulomb interaction in spin-zero limit $a_{\pm} \rightarrow 0$.

As special cases, we consider the spins of interacting magic fields being either aligned equal $a_{\pm} = a$ as well as anti-aligned equal $a_{\pm} = \pm a$ in side-by-side configuration. For both cases, we have $f = f_0 := \frac{1}{2}\sqrt{d^2 - 4a^2}$ and $e = 0$. In the aligned case, we obtain

$$U_{\text{SS}} \Big|_{a_{\pm}=a} = (q_+ q_-) \frac{1}{2f_0} = (q_+ q_-) \frac{1}{\sqrt{d^2 - 4a^2}}, \quad (3.53)$$

whereas in the anti-aligned case, we have

$$U_{\text{SS}} \Big|_{a_{\pm}=\pm a} = (q_+ q_-) \frac{1}{d}. \quad (3.54)$$

The interaction potential in aligned case (3.53) is depicted in Figure 11c and 11d for charges having the same or opposite signs, respectively.

4 Conclusion and Discussion

The paper is devoted to the analysis of the electromagnetic magic field, the $G \rightarrow 0$ limit of the Kerr-Newman solution of Einstein-Maxwell equations and its interactions. We have analyzed the analytic continuation of the complex potential for a single magic field, as well as the superposition of two such fields. Although the self-energy of the magic field diverges, its Lagrangian is finite. This feature, which is contrary to the Coulomb field, admits the derivation of the interaction potential from the total Lagrangian of the superposed fields.

The interaction potential of two magic fields has the Coulomb potential as the leading order term for large distances with corrections due to the spin parameters appearing at order $1/d^3$. For small distances,

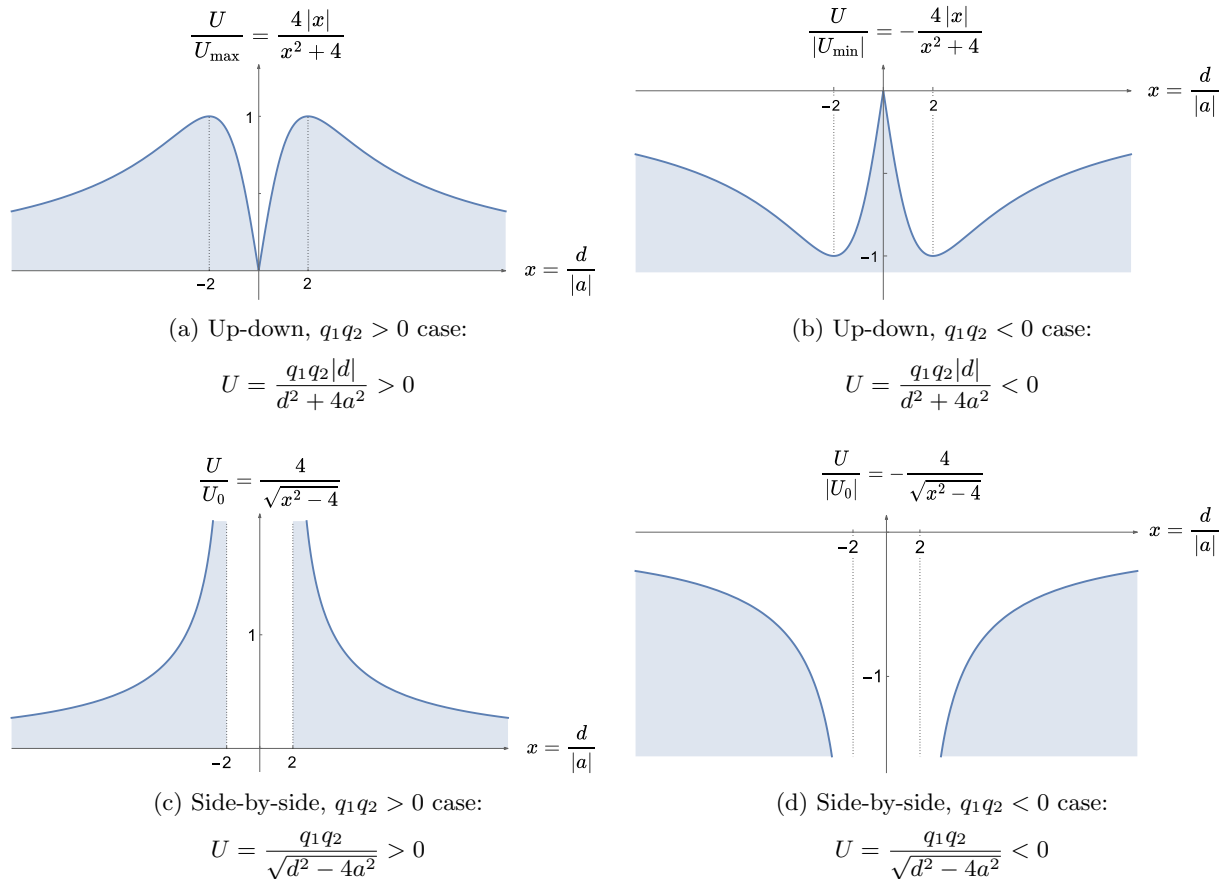


Figure 11: The interaction potential $U = \mathcal{L}_{\text{int}}$ of two magic fields in up-down and side-by-side configurations for $q_1 q_2 > 0$ and $q_1 q_2 < 0$ cases, where the spin parameters are the same and aligned. In the up-down case, the interaction potential is normalized to the absolute value of its extremum, and in the side-by-side case to $U_0 = q_1 q_2 / 4|a|$.

there is a qualitative difference from the Coulomb case. For some configurations, we find, in contrast to the Coulomb interaction potential, a potential well with a diameter comparable to the spin a of the field.

The work in this paper raises several questions that will be addressed in future work. As has been discussed above, the nature of the Kerr-Newman solution and the magic field exhibit several interesting analogies with the electron. The lowest electromagnetic multipole moments of the magic field and those of the electron are closely similar, which raises questions about the higher multipole moments of the electron, which yet have to be measured experimentally, as well as the role of the self-gravitating nature of the electron in determining its multipole structure. Here, one may draw an interesting parallel to uniqueness results for stationary electrovac black holes.

The analogy with the electron is further emphasized by the fact that the analytic continuation of the magic field exhibits spin-1/2 features, demonstrated by the 4π angle needed to go around the singularity, cf. Figure 4 and the discussion around it. The scale of the potential well found in the interaction potential could lead to an analogy of electron-positron pairs as well as orbiting configurations. These issues will be further discussed in a separate paper, where also the motion of the system of two magic fields will be considered.

Finally, it is worth mentioning the fact that the magic field is related to infinitesimal Kerr by the double copy procedure. There is a close analogy between linearized gravity and electromagnetism [30,31]. From this point of view, it is interesting to consider the interaction potential for infinitesimal Kerr and its implications for the post-Minkowskian black hole scattering problem [32–34].

Acknowledgement

KR thanks Lars Samuelsson and Mikael von Strauss for their valuable contributions at the early stages of this project. SA & LA thank the Institut Henri Poincaré (IHP), where part of this work was carried out during

the program Quantum and Classical Fields Interacting with Geometry. SA is supported by the Humboldt Research Fellowship.

References

- [1] Brandon Carter. Global Structure of the Kerr Family of Gravitational Fields. *Physical Review*, 174(5):1559–1571, October 1968.
- [2] Steven Weinberg. *The quantum theory of fields. Vol. I*. Cambridge University Press, Cambridge, 2005. Foundations.
- [3] D. Lynden-Bell. *A magic electromagnetic field*. Chapter 25 in *Stellar Astrophysical Fluid Dynamics* p. 369-376. Cambridge Univ. Press, 2003.
- [4] Brandon Carter. Killing tensor quantum numbers and conserved currents in curved space. *Phys. Rev. D*, 16:3395–3414, Dec 1977.
- [5] W. Dietz and C. Hoenselaers. Two mass solutions of Einstein’s vacuum equations: The double Kerr solution. *Annals of Physics*, 165:319–383, 1985.
- [6] Arthur N. Cox, editor. *Allen’s Astrophysical Quantities*. Springer Science+Business Media New York, 4th edition, 2002.
- [7] V Andreev et al. Acme. *Improved limit on the electric dipole moment of the electron*. *Nature*, 7727:355–360, 2018.
- [8] Tanya S. Roussy, Luke Caldwell, Trevor Wright, William B. Cairncross, Yuval Shagam, Kia Boon Ng, Noah Schlossberger, Sun Yool Park, Anzhou Wang, Jun Ye, and Eric A. Cornell. An improved bound on the electron’s electric dipole moment. *Science*, 381(6653):46–50, July 2023.
- [9] J. J. Sakurai and Jim Napolitano. *Modern Quantum Mechanics*. 2020.
- [10] Arthur H. Compton. The Size and Shape of the Electron. *Physical Review*, 14(3):247–259, September 1919.
- [11] J. V. Koski, A. J. Landig, M. Russ, J. C. Abadillo-Uriel, P. Scarlino, B. Kratochwil, C. Reichl, W. Wegscheider, Guido Burkard, Mark Friesen, S. N. Coppersmith, A. Wallraff, K. Ensslin, and T. Ihn. Strong photon coupling to the quadrupole moment of an electron in a solid-state qubit. *Nature Physics*, 16(6):642–646, May 2020.
- [12] Kjell Rosquist. Gravitationally induced electromagnetism at the compton scale. *Classical and Quantum Gravity*, 23(9):3111–3122, April 2006.
- [13] P. Appell. Quelques remarques sur la théorie des potentiels multiformes (some remarks on the theory of multiform potentials). *Mathematische Annalen*, 30(1):155–156, 1887.
- [14] A. Sommerfeld. Über verzweigte potentiale im raum. *Proceedings of the London Mathematical Society*, 1(1):395–429, 1896.
- [15] John Lighton Synge. *Relativity: the special theory*, 1956.
- [16] Donald Lynden-Bell. On why discs generate magnetic towers and collimate jets. *Monthly Notices of the Royal Astronomical Society*, 341(4):1360–1372, 2003.
- [17] E. T. Newman and A.I. Janis. Note on the kerr spinning-particle metric. *Journal of Mathematical Physics*, 6(6):915–917, 1965.
- [18] N. Arkani-Hamed, Y-T. Huang, and D. O’Connell. Kerr black holes as elementary particles. *Journal of High Energy Physics*, 2020(1):1–12, 2020.
- [19] R. Monteiro, D. O’Connell, and C. D. White. Black holes and the double copy. *Journal of High Energy Physics*, 2014(12):56, December 2014.

- [20] Iwo Białynicki-Birula and Zofia Białynicka-Birula. The role of the riemann–silberstein vector in classical and quantum theories of electromagnetism. *Journal of Physics A: Mathematical and Theoretical*, 46(5):053001, jan 2013.
- [21] Michael K.-H. Kiessling and A. Shadi Tahvildar-Zadeh. On the quantum-mechanics of a single photon. *Journal of Mathematical Physics*, 59(11):112302, 11 2018.
- [22] Frederick J. Ernst. New formulation of the axially symmetric gravitational field problem. *Phys. Rev.*, 167:1175–1178, Mar 1968.
- [23] A S. Tahvildar Zadeh. On a zero-gravity limit of the Kerr–Newman spacetimes and their electromagnetic fields. *Journal of Mathematical Physics*, 56(4):042501, 2015.
- [24] Donald Lynden-Bell. A magic electromagnetic field, 2002.
- [25] D. Lynden-Bell. Electromagnetic magic: The relativistically rotating disk. *Phys. Rev. D*, 70(10):105017, 2004.
- [26] G. Kaiser. Distributional sources for Newman’s holomorphic Coulomb field. *J. Phys. A: Math. Theor.*, 37(36):8735, 2004.
- [27] David M. Zipoy. Topology of some spheroidal metrics. *Journal of Mathematical Physics*, 7(6):1137–1143, 06 1966.
- [28] Gary W. Gibbons and Mikhail S. Volkov. Ring wormholes via duality rotations. *Physics Letters B*, 760:324–328, 2016.
- [29] Kjell Rosquist, Lars Samuelsson, and Mikael von Strauss. Interacting Kerr-Newman Fields. In Ali H. Chamseddine, editor, *Twelfth Marcel Grossmann Meeting on General Relativity*, pages 2041–2043, January 2012.
- [30] Stephen M Barnett. Maxwellian theory of gravitational waves and their mechanical properties. *New Journal of Physics*, 16(2):023027, feb 2014.
- [31] Sajad Aghapour, Lars Andersson, and Reebhu Bhattacharyya. Helicity and spin conservation in linearized gravity. *General Relativity and Gravitation*, 53:1–11, 2021.
- [32] Thibault Damour. Gravitational scattering, post-minkowskian approximation, and effective-one-body theory. *Phys. Rev. D*, 94:104015, Nov 2016.
- [33] Justin Vines. Scattering of two spinning black holes in post-minkowskian gravity, to all orders in spin, and effective-one-body mappings. *Classical and Quantum Gravity*, 35(8):084002, mar 2018.
- [34] Justin Vines, Jan Steinhoff, and Alessandra Buonanno. Spinning-black-hole scattering and the test-black-hole limit at second post-minkowskian order. *Phys. Rev. D*, 99:064054, Mar 2019.